Non-destructive Electron Microscopy through Interaction-free Quantum Measurement

by

William P. Putnam

Submitted to the Department of Electrical Engineering and Computer Science
in partial fulfillment of the requirements for the degree of

Master of Engineering in Electrical Engineering and Computer Science

at the

MASSACHUSETTS INSTITUTE OF TECHNOLOGY

June 2008

© William P. Putnam, MMVIII. All rights reserved.

The author hereby grants to MIT permission to reproduce and distribute publicly paper and electronic copies of this thesis document in whole or in part.

MASSACHUSETTS INSTITUTE OF TECHNOLOGY
JUL 20 2009
LIBRARIES

Author .....
Department of Electrical Engineering and Computer Science
May 23, 2008

Certified by .....
Mehmet Fatih Yanik
Assistant Professor
Thesis Supervisor

Accepted by .....
Arthur C. Smith
Chairman, Department Committee on Graduate Students

ARCHIVES

Non-destructive Electron Microscopy through Interaction-free Quantum Measurement

by

William P. Putnam

Submitted to the Department of Electrical Engineering and Computer Science
on May 23, 2008, in partial fulfillment of the
requirements for the degree of
Master of Engineering in Electrical Engineering and Computer Science

Abstract

In this thesis, the possibility of interaction-free quantum measurements with electrons is investigated. With a scheme based on existing charged particle trapping techniques, it is demonstrated that such interaction-free measurements are possible in the presence of previously measured quantum decoherence rates, and the efficiency of the measurement scheme and the absorption probability are estimated. Use of such interaction-free measurements with electrons in imaging applications could dramatically reduce sample damage induced by electron-exposure, which might allow non-destructive, molecular-resolution electron microscopy.

Thesis Supervisor: Mehmet Fatih Yanik
Title: Assistant Professor

Acknowledgments

I would like to thank my advisor Fatih Yanik. I could not have completed this project without his helpful discussions and guidance.

Contents

List of Figures

Chapter 1

Introduction

Since the development of the first prototype in the early twentieth century, the electron microscope has revolutionized the field of microscopy and has dramatically impacted many areas of science and engineering. Typical optical microscopy techniques are limited by the diffraction barrier which constrains the achievable resolution to roughly the wavelength of the probing light (optical wavelengths range from around 380 nm to 750 nm). Although cutting-edge optical techniques such as Stimulated Emission Depletion (STED) can now provide resolutions beyond the constraints of the diffraction barrier, the nanometer or even sub-nanometer scale resolution provided by electron microscopes gives scientists and engineers the capability of imaging at length scales currently inaccessible by even the most advanced optical techniques.

The earliest electron microscopes functioned much like simple optical microscopes, in a transmission mode; a beam of electrons was directed towards and penetrated a thin sample. The electrons were then focused to form an image by electron optics (specially designed coils and plates that deflect electron beams via electromagnetic and electric forces in a fashion analagous to how lenses deflect optical beams) [1]. These transmission electron microscopes (TEMs) and the field of electron microscopy have evolved considerably since their inception, and nowadays there exist a wide variety of different TEM techniques involving high voltages and complicated sample preparation protocols as well as other wholly different methods of electron microscopy such as scanning electron microscopy. Scanning electron microscopes (SEMs) do not

rely on the transmission of the incident electron through the sample but instead use secondary electrons produced by the interaction of the incident electron beam with the sample's surface to generate an image. This variety of different techniques has allowed imaging down to near atomic scales of a wide spectrum of samples ranging from semiconductor nanostructures to specially prepared biological specimens.

Despite the great successes of electron microscopy, the application of the technique to the investigation of biological phenomena or other sensitive specimens has been limited due to constraints related to the fundamental principle on which the microscopes operate. Modern electron microscopes still follow the same basic paradigm of their predecessors: electron beams impinge upon a sample and interact through transmission, auxilary electron production, etc. Through this interaction information about the sample is obtained and an image is constructed; however, also through this interaction the sample is damaged by the energetic incident electrons.

The electrons used in electron microscopy have variable energy levels; however, for the best imaging energies in the range of keV (and MeV for high-voltage TEMs) are commonly used [1]. When biological specimens are irradiated by electron beams of these energies molecular excitation, ionization, and subsequent chemical reactions occur damaging the structures of the biological complexes [2]. The required electron exposure, equivalent radiation dosage, and resulting effects for imaging certain biological specimens with a high-voltage TEM at 1 MeV are given in Figure 1-1.

As is evident in Figure 1-1, the radiation received by samples imaged by electron microscopes is excessive in biological terms. It has been determined that during the recording of a single micrograph a specimen can receive a radiation dosage equivalent to being roughly thirty yards from the explosion of a ten megaton Hydrogen bomb or to spending five years near a 1-Ci Co^{60} γ-ray source [3]. In recent years new techniques in sample preparation such as cryogenic preparation [4] have allowed improved imaging of biological samples, yet the problem of radiation damage still remains a major one, and the ability to image living, not dying, biological samples still remains out of reach.

In the following thesis, the possibility of interaction-free quantum measurements

Radiation Damage at 1 MV

Resolvable Structures (assuming 10% contrast)	Required Electron Exposure (C/cm^2)	Biological Effect
Whole cell (10 μm)	10^{-10}—10^{-9}	Reproductive Cell Death (animal cells)
Cell nucleus (2 μm)	10^{-8}	Inactivation of T1 bacteriophage
Tumor virus (100 nm)	10^{-6}—10^{-5}	Enzyme Inactivation
Ribosomes (20 nm)	10^{-4}	Stoppage of cell motility (protozoa)
Cell membranes (10 nm)	10^{-4}—10^{-3}	
Enzymes (5 nm)	10^{-3}—10^{-2}	
1 nm resolution	10^{-2}—10^{-1}	

Figure 1-1: Imaging Requirements and Radiation Damage in Electron Microscopy

with electrons is investigated. Interaction-free quantum measurement is a peculiar manifestation of quantum non-locality and interference which can allow detection without interaction. The application of interaction-free measurements with electrons could dramatically reduce sample damage in electron microscopy by circumventing the seemingly fundamental restriction of electron microscopes: interaction.

Before going directly into a complete discussion of interaction-free quantum measurement and difficulties in applying the method to electron based applications, it is instructive to first present the fundamental ideas of the concept through a simple and familiar example: the double-slit experiment. This instructive introduction is provided in the following section as well as an outline of the rest of the thesis.

1.1 Imaging with Double-slit Interferometery

From classical intuition, any measurement on an object requires some physical interaction with the object. As discussed, for electron microscopy this interaction has made the imaging of sensitive samples extremely challenging [5]. Quantum mechan-

ical intuition does not seem to change this fact. From quantum mechanics it seems that any measurement inevitably changes the state of the system. However, as will be discussed in more detail in the following chapter this is not always the case. A simple example illustrating these principles can be found in the well-known double-slit experiment.

Take a double-slit apparatus illuminated by a beam of single photons (that is a beam which consists of one photon following another) as illustrated in Figure 1-2 (the apparatus could equally well be illuminated by single electrons in which the double-slit could be a filament at a negative voltage followed by a focusing apparatus). From basic quantum mechanics when the two slits are illuminated by the beam of single photons (as in the top of Figure 1-2), an interference pattern will form on the detector as each photon traverses the two slits simultaneously, interferes with itself, and deposits its energy on the detector to the far right (this is a quantum mechanical effect as the discussion is focusing on a beam of single photons not a classical light beam).

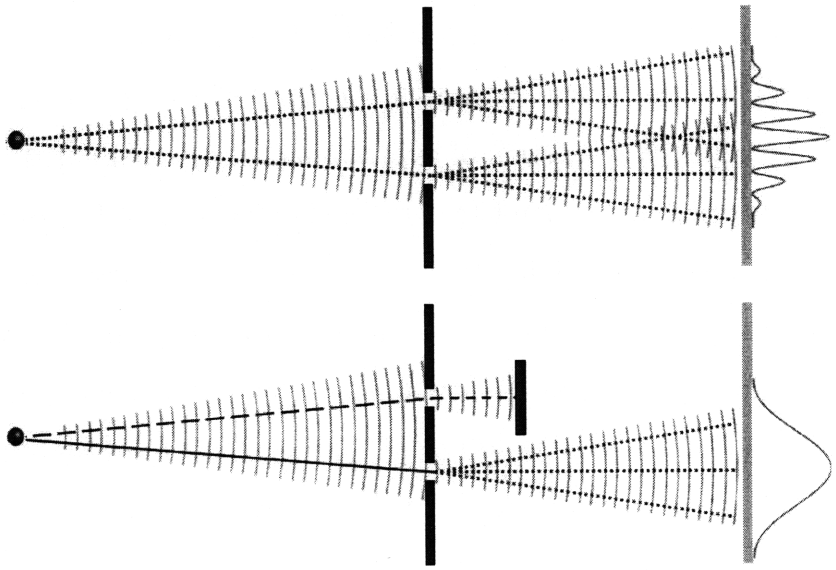

Figure 1-2: Double-slit experiment. The balls and dashed trajectories are meant to emphasize the particle-like nature of the photon, and the wavefronts are meant to emphasize the photon's wave-like properties. The patterns on the far right are meant to represent the spatial variation in the intensity after many photons have traveled through the simple interferometer.

If one of the slits is blocked by an absorbing object (as in the bottom of Figure 1-2) however, then the interference pattern will not be observed at the detector (although a weak diffraction pattern may be seen). This is because the absorbing object enacts a measurement on each photon's wavefunction determing whether the photon traversed the top or bottom slit. If the top slit is the result of the measurement, the photon's energy is then imparted to the absorbing object. If the bottom slit is the result, then the photons energy is then spread on the detector screen (with some weak diffraction due to the propagation from where the measurement was enacted to the detector).

Now imagine that an object is being imaged by this simple double-slit apparatus. Take the object to be composed of dark, i.e. absorbing or opaque, and white, i.e. not absorbing or transparent, pixels. If the object is rastered slowly enough across the top slit, then at the detector occasionally interference patterns will be observed corresponding to transparent regions of the object or white pixels in front of the slit, and occasionally interference patterns will not be seen corresponding to opaque regions of the object or black pixels in front of the slit. In this way a simple black and white image of the object can be generated.

What is particularly interesting about this double-slit imaging is that the imaged object is exposed to only half the light intensity it would be in a classical transmission imaging apparatus. When a dark pixel is imaged, roughly half of the total number of incident photons travel the path without the object to form the classical intensity pattern on the detector, and roughly half of the total number of incident photons travel the path with the object to be absorbed. In a typical transmission imaging setup however all of the incident photons would be absorbed by the dark pixel. Therefore, the double-slit imaging system discussed above exploits quantum interference to reduce the exposure of the sample to photons by roughly a factor of two (with obvious loss of contrast however).

This double-slit imaging system is in essence an interaction-free quantum measurement/imaging (IFM) system. In Chapter 2 interaction-free quantum measurement will be discussed in greater detail, and other schemes, including one for imaging with electrons will be disussed. In Chapter 3 a coupled electron trap design which may

be capable of carrying out electron based interaction-free measurements or even microscopy will be presented and analyzed. Then in Chapter 4 the major limiting factors in the design will be presented along with an analysis of the potential performance of the imaging system. Finally, Chapter 5 will include conclusions and a brief outlook on future work.

Finally, before jumping into the following chapters it should be noted that this thesis is not a complete and detailed account of the work done by the author in this area to date. This thesis is more of an abbreviated description of the ideas and relevant calculations and serves the purpose to instruct an audience in a broader sense rather than to list in painful detail every calculation. Important details have been glossed over in many cases for brevity and clarity in the presentation. For more details on particular simulations or calculations the author may be contacted.

Chapter 2

Interaction-free Quantum Measurement

As mentioned in the preceding chapter, classical and quantum intuition both seem to imply that a measured system is always affected by the measurement process. However, as illustrated with a simple thought experiment involving a double-slit interferometer, quantum interference may be exploited to reduce the "amount" of interaction ("amount" of interaction refers to amount of energy exchanged in interaction) involved in a particular measurement (in the previous example the number of photons absorbed by the measured object was reduced by a factor of two). As it turns out, with slightly more clever interferometric techniques quantum interference can be used to reduce the "amount" of interaction (energy exchange in interaction) to zero. In the discussion in the following chapter these more clever interferometric techniques will be discussed. The canonical Mach-Zehnder interaction-free measurement protocol will be presented as a standard introduction to interaction-free quantum measurement. A specific high-efficiency interaction-free measurement setup will then be discussed along with it's key ingredient: the quantum Zeno effect. Finally, general high-efficiency interaction-free measurement with two-state systems will be analyzed, and a basic setup for interaction-free measurment with electrons will be presented.

2.1 The Mach-Zehnder Implementation

Interaction-free measurement is commonly traced back to a famous set of "negative-result" thought experiments in which the non-observance of a particular result acts itself as a measurement that leaves the system undisturbed i.e. an interaction-free measurement [6]. These thought experiments were later extended into a realistic measurement scheme involving a Mach-Zehnder interferometer [7]. This Mach-Zehnder scheme has become the classic example of interaction-free measurement, so fittingly it is discussed here before more involved schemes are analyzed.

In accordance with its name the Mach-Zehnder interaction-free measurement scheme conists simply of a tuned Mach-Zehnder interferometer with an incident beam of single photons. The setup is illustrated in Figure 2-1. The interferometer has the bottom or top arm either open or blocked by the object being measured (on the left in Figure 2-1 the bottom arm is open, on the right it is blocked). To make things dramatic, in the original proposal [7] the objects imaged in the thought experiment were bombs (as in Figure 2-1) with single photon detectors as triggers, and the idea was to distinguish operational weapons from duds.

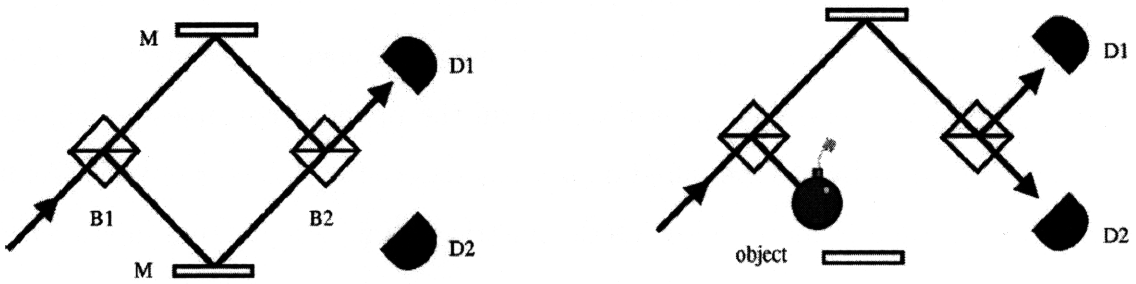

Figure 2-1: The Mach-Zehnder Interferometer and Interaction-free Measurement [8]. The label "M" indicates a mirror, the label "B" indicates a beam-splitter, and the label "D" indicates a detector. The dark line and arrow indicate the path of the photons in the interferometer.

Let the reflectivity, R_1, of the first beam-splitter equal the transmistivity, T_2, of the second, and let the relative phase shift be $\pi/2$ between a wave reflected and transmitted by the beam-splitter (this phase shift need not be π because the reflection

could be a result of a series of complex internal reflections in a thin dielectric slab [9]).

With both arms open (the left in Figure 2-1) the relative phase shift between a photon traveling through the bottom arm versus the top arm and reaching detector D1 is $\pi/2 - \pi/2 = 0$ while the relative phase shift between a photon traveling through the bottom arm versus the top arm and reaching detector D2 is $\pi/2 + \pi/2 = \pi$. So with both arms open the there will be complete destructive interference (note the importance of $R_1 = T_2$ here) at detector D2 i.e. no photons will be measured at D2 and constructive interference at D1 i.e. every photon sent into the interferometer will be measured at D1 (assuming no losses).

If an object, which is assumed to be a perfect absorber, is placed in the bottom arm of the interferometer (the right in Figure 2-1) the interference is lost. As in the case with the double-slit interferometer the absorbing object enacts a measurement on each photon and partially collapses each incident photon's wavefunction to one arm of the interferometer (in the case illustrated above the top arm). Therefore, the incident photon can now be measured at either detector D1 or D2.

The discussion so far has all been simple, straightforward quantum mechanics; however, it becomes interesting when one notes that if a single photon is sent into the Mach-Zehnder interferometer and is measured at D2, then there must be an object in the bottom arm of the interferometer and the photon must never have interacted (exchanged energy) with it [7]. So, the presence of an object can be detected without ever interacting with the object.

A simple efficiency figure of merit can be defined for this interaction-free measurement system. The efficiency can be defined as the probability of correctly determining the presence or absence of an object blocking the bottom arm of the interferometer [10]. Assuming the *a priori* probabilities of there being a blocking object are $P(\text{present}) = P(\text{absent}) = \frac{1}{2}$, the efficiency can be written,

$$\eta = \frac{1}{2}(P(\text{D1}|\text{absent}) + P(\text{D2}|\text{present})) \tag{2.1}$$

Where $P(\text{D1}|\text{absent})$ and $P(\text{D2}|\text{present})$ denote the probability of measuring a photon at D1 and D2 given the absence of an object and the presence object respectively. From the above discussion clearly $P(\text{D1}|\text{absent}) = 1$ as with no object present there is complete destructive interference at D2. Also from the above discussion, $P(\text{D2}|\text{present}) = (1 - R_1)T_2 = (1 - R_1)R_1$. Using these expressions the efficiency is rewritten below and the maximum efficiency can easily be seen to be $\eta_{max} = 3/4$ with $R_1 = 1/2$.

$$\eta = \frac{1}{2}(1 + R_1 - R_1^2) \tag{2.2}$$

One other figure of merit is important in characterizing the interaction-free measurement system. That is the probability of absorption by the object P_{abs}. For the above system the absorption probability is clearly $P_{abs} = R_1$, and so for the case of maximum efficiency $P_{abs} = 1/2$. For an interaction-free imaging system the exposure the imaged sample receives is proportional to the absorption probability, so for an electron microscopy system based on the above scheme the electron exposure would be reduced by a factor of two (when operating at maximum efficiency).

This system is the canonical example of interaction-free measurement. Its counterintuitive results have been verified experimentally with phtons and neutrons in Mach-Zehnder structures [11, 12, 13]. Although important from a pedagogical point of view, the system has clear deficiences. In particular, $\eta \leq 3/4$ and as this limit is approached $P_{abs} \rightarrow 1/2$. For interaction-free measurement to be practical in reducing sample exposure in electron microscopy a more efficient implementation with less absorption is necessary.

2.2 High-Efficiency IFM

Making use of one of the odder effects in quantum dynamics: the quantum Zeno effect, an IFM scheme with efficiency arbitrarily close to unity and absorption negligibly small can be devised. In the following section a simple phenomenological discussion of the quantum Zeno effect (paralleling the discussion in [14]) is presented and then a particular high-efficiency IFM system [15] is introduced.

2.2.1 The Quantum Zeno Effect

The quantum Zeno effect is the inhibition of quantum transitions by frequent measurement. The result is counterinuitive yet arises simply as a dynamical effect of unitary evolution [14]. Consider a system prepared in a state $|u\rangle$ at some initial time $t = 0$. Evolution according to the Schrödinger equation will lead to a superpostion of this initial state with some collection of orthogonal states $|v_k\rangle$ with respective amplitude $a_u(t)$ and $a_{v_k}(t)$,

$$|\Psi(t)\rangle = a_u(t)\,|u\rangle + \sum_{v_k \neq u} a_{v_k}(t)\,|v_k\rangle \tag{2.3}$$

The probability of finding the system in the initial state at a later time $t > 0$ is then,

$$P(t) = |a_u(t)|^2 = |\,\langle u|\exp(-iHt)\,|u\rangle\,|^2 \tag{2.4}$$

Expanding the exponential in powers of t,

$$P(t) = 1 - (\Delta H)^2 t^2 + O(t^4) \tag{2.5}$$

Where $(\Delta H)^2 = \langle u|\,H^2\,|u\rangle - \langle u|\,H\,|u\rangle^2$. Now making N measurements in some time interval (with N large enough to neglect the $O(t^4)$ term), the probability of finding the system in the initial state is,

$$\begin{aligned} P(t) &\approx \left(1 - (\Delta H)^2 \left(\frac{t}{N}\right)^2\right)^N \\ &\approx 1 - (\Delta H)^2 \frac{t^2}{N} + \ldots \\ &\approx 1 \end{aligned}$$

The last approximation holds as N goes to infinity. So, from the simple argument above, repeated measurements can inhibit the evolution of a system. This is the essence of the quantum Zeno effect.

2.2.2 The High-Efficieny IFM Interferometer

The quantum Zeno effect is central in high-efficiency interaction-free measurement as the measured object will enact repeated measurements on the wavefunction of the interrogating photons or electrons and a quantum Zeno type effect will determine the outcome of the IFM. Consider the particular interferometer displayed in Figure 2-2.

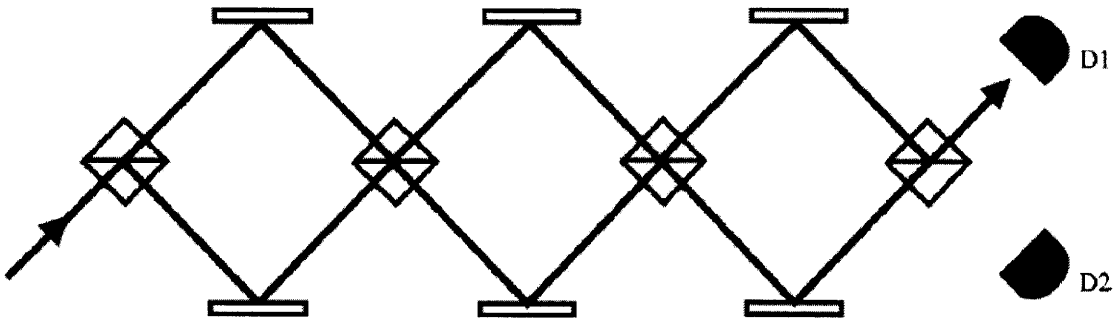

Figure 2-2: High-efficiency Interaction-free Measurement [8]. The image shows an interferometer that implements the high-efficiency, quantum Zeno IFM protocol for $N_{BS} = 4$. Again the flats represent mirrors, the boxes represent beam-splitters, the "D's" represent detectors, and the black lines and arrows represent the direction and propagation of single photons.

Let the number of beam-splitters in the interferometer be N_{BS} (in the above case $N_{BS} = 4$). Then let the reflectivity of each beam-splitter be $R_{BS} = \cos^2(\pi/2N_{BS})$ (the transmittance of each beam-splitter is then $T_{BS} = \sin^2(\pi/2N_{BS})$). A photon in the lower arm of interferometer is described by the ket $|L\rangle$, and a photon in the upper arm the system is described by $|U\rangle$. A photon in the state $a|L\rangle + b|U\rangle$ is transformed by one of the beam-splitters like,

$$a|L\rangle + b|U\rangle \rightarrow (a\sqrt{R_{BS}} + b\sqrt{T_{BS}})|L\rangle + (a\sqrt{T_{BS}} + b\sqrt{R_{BS}})|U\rangle \tag{2.6}$$

Since $a^2 + b^2 = 1$, one can write $a = \cos\theta$ and $b = \sin\theta$. Then plugging these expressions in to the above equation and using the specified values of R_{BS} and T_{BS} one finds that each beam-splitter transforms the system like,

$$\begin{aligned}\cos\theta\,|L\rangle + \sin\theta\,|U\rangle \;&\rightarrow\; (\cos\theta\cos(\pi/2N_{BS}) + \sin\theta\cos(\pi/2N_{BS}))\,|L\rangle \\ &\quad +(\cos\theta\sin(\pi/2N_{BS}) + \sin\theta\cos(\pi/2N_{BS}))\,|U\rangle \\ &= \cos(\theta - \pi/2N_{BS})\,|L\rangle + \sin(\theta + \pi/2N_{BS})\,|U\rangle\end{aligned}$$

The operation of each beam-splitter is analgous to a rotation operator that rotates the state vector of the system (in the $|L\rangle, |U\rangle$ basis) by an angle of $\pi/2N_{BS}$. Therefore, going through N_{BS} beamsplitters is equivalent to cascading N_{BS} rotation matrices, so the system will be rotated by $\pi/2$ radians in the the $|L\rangle, |U\rangle$ basis. So, a photon entering in the lower arm of the interferometer, as in Figure 2-2 (that is with an initial state of $|L\rangle = \cos(0)\,|L\rangle + \sin(0)\,|U\rangle$) will emerge from the N_{BS} beam-splitters in the upper arm of the interferometer (in state $|U\rangle = \cos(\pi/2)\,|L\rangle + \sin(\pi/2)\,|U\rangle$).

It is clear then that for a single photon initially starting in the lower arm of the interferometer (state $|L\rangle$) propagation through N_{BS} beam-splitters will result in destructive interference at detector D2, and photons will only be measured at D1 (the state of the photon after N_{BS} beam-splitters is $|U\rangle$). However, like in the Mach-Zehnder implementation, if a perfect absorber is placed in the upper arm of every interferometer this destructive interference is destroyed, and the probability of measuring the photon emerging from detector D2 becomes $P(\text{D2}|\text{present}) = R^N_{BSBS} = \cos^{2N_{BS}}(\pi/2N_{BS})$. This measurement of a photon at D2 then consitutes an interaction-free measurement of an object in the upper arm of the interferometer. (Although in the illustration it appears that an object would need to be inserted above each beam-splitter, in actual implementations [15] photons are cycled through a single beam-splitter).

The efficiency of the interaction-free measurement and the probability of the object absorbing a photon can now be calculated. From the preceeding discussion it is clear that $P(\text{D1}|\text{absent}) = 1$ and $P(\text{D2}|\text{present}) = \cos^{2N_{BS}}(\pi/2N_{BS})$. So, the efficiency can be written (again assuming equal *a priori* probabilities of the absence and presence of an object),

$$\begin{aligned} \eta &= \frac{1}{2}(1+\cos^{2N_{BS}}(\pi/2N_{BS})) \\ &\approx 1-\frac{\pi^2}{8N_{BS}} \end{aligned} \tag{2.7}$$

The second expression is a Taylor expansion of the first for large N_{BS}. So, clearly the efficiency approaches unity as the number of beam-splitters grows. So with arbitrarily high probability the above scheme can be used to determine the presence of absence of an absorbing object without interaction. The probability of absorption can be calculated to be,

$$\begin{aligned} P_{abs} &= T_{BS}+R_{BS}T_{BS}+R_{BS}^2T_{BS}+...+R_{BS}^{N_{BS}-2}T_{BS} \\ &= \sin^2(\pi/2N_{BS})\sum_{k=0}^{N_{BS}-2}\cos^{2k}(\pi/2N_{BS}) \\ &\approx \frac{\pi^2}{4N_{BS}} \end{aligned} \tag{2.8}$$

So as N_{BS} grows very large, the absorption probability goes to zero. Clearly, the above system meets the necessary requirements for effective interaction-free imaging: high-efficiency and low absorption probability.

Stepping back from the details, the operation of this system can easily be understood physically. The reflectivity of each beam-splitter is high, or thinking of the interferometer as a two-state system, the coupling between the two-states is small. So, only a small portion of the photon wavefunction will transmit at the beam-splitters. The small portion that transmits will then be absorbed by the object. However, since only a small amplitude transmits the probability that the object actually measures the presence of the photon and absorbs it is very small. Instead the interaction with the object just collapses the small transmitted amplitude and restores the wavefunction to its original state. This repeated collapse to the initial state is the quantum Zeno Effect in action. The above system has been experimentally developed using

photon polarization states, and efficiencies of 73% have been observed [15]. Additionally, a similar high-efficiency IFM system has been proposed and experimentally demonstrated in a simple Fabry-Perot structure with similar efficiencies [16, 10].

2.3 Two-state IFM and Electrons

As alluded to at the end of the preceeding section, the only requirement for a high-efficiency, quantum Zeno IFM scheme is a two-state system. To reinforce this point, consider a simple 2x2 Hamiltonian with diagonal elements E and off-diagonal, coupling elements $\hbar\Delta$. The Hamiltonian will have symmetric, $|\psi_s\rangle$, and anti-symmetric eigenstates, $|\psi_a\rangle$, with energies $E_s = E - \hbar\Delta$ and $E_a = E + \hbar\Delta$ respectively. From basic quantum mechanics, the evolution of such a system goes as,

$$H = \begin{pmatrix} E & \hbar\Delta \\ \hbar\Delta & E \end{pmatrix} \Rightarrow \psi \sim \begin{pmatrix} \cos(\Delta t) \\ \sin(\Delta t) \end{pmatrix} \tag{2.9}$$

The general high-efficiency IFM protocol is formed by applying the quantum Zeno effect to this system. The protocol is as follows. Prepare the system in one of the projection states, that is in one of the superposition states $\frac{1}{\sqrt{2}}(|\psi_s\rangle \pm |\psi_a\rangle)$ (in the context of a double-well, these are the classical-looking spatially localized states). Let the system evolve for some small period of time then interrupt the evolution with an object and repeat this process. Finally, at $t = \pi/2\Delta$ measure the state of the two-state system. If the object is transparent the evolution will have been left alone and the system will have evolved into the other projection state. However, if the object is opaque the system's coherent evolution will have been repeatedly inhibited and, with very high probability (if the repetition rate is made high enough), the system will be in the initial projection state as predicted by the quantum Zeno effect.

This general two-state IFM protocol can be applied to a two-state system with electrons. Consider two ring shaped electron guides each with radius R and vertically stacked with a separation of Δz as shown in Figure 2-3. The ring shaped electron guides create a two-dimensional confining potential in the $\vec{r}$ and $\vec{z}$ directions that

restricts the motion of electrons solely to the tangential direction along the circumferences of the rings i.e. the $\vec{\theta}$ direction. The potential $U_{eff}(r,z)$ corresponds to this confining potential and also couples the two ring shaped guides with a double-well potential in the $\vec{z}$ direction.

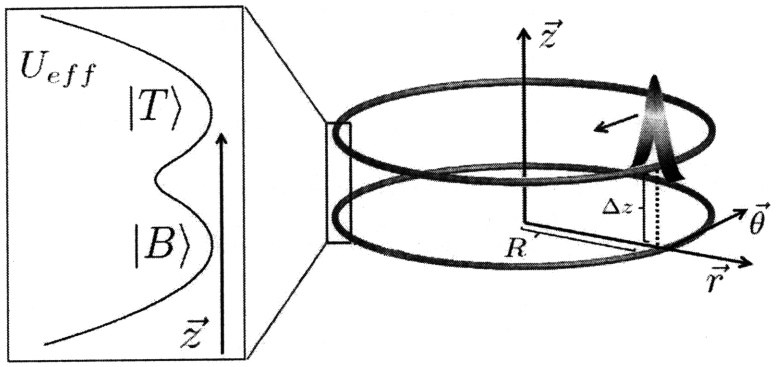

Figure 2-3: Coupled Electron Ring Guides. The colorful wavepacket illustrates the amplitude of the circulating electron. The guide potential $U_{eff}(r,z)$ couples the localized electron states $|T\rangle$ and $|B\rangle$ in a double-well potential.

Due to the double-well potential in the $\vec{z}$ direction, the two lowest energy states of the electron in the r-z plane (i.e. the transverse ground and first excited states) correspond to a symmetric state $|\Psi_s\rangle$ with energy E_s and an anti-symmetric state $|\Psi_a\rangle$ with energy E_a. States which correspond to spatial localization of the electron in the top ring and the bottom ring can be expressed as $|T\rangle = (|\Psi_s\rangle + |\Psi_a\rangle)/\sqrt{2}$ and $|B\rangle = (|\Psi_s\rangle - |\Psi_a\rangle)/\sqrt{2}$ respectively. As expected these states are similar to those that exist for the simple 2x2 Hamiltonian discussed above.

When the energy splitting $2\hbar\Delta \equiv E_a - E_s$ is sufficiently small, the double-well can be approximated as a two-state system. Then the circularly propagating electron in Figure 2-3, initially prepared in a localized state in the top ring, undergoes undamped oscillations between the states $|T\rangle$ and $|B\rangle$ (in agreement with the time dependence of the simple two-state system discussed previously).

The time-dependent probabilities of the electron occupying the top versus the bottom rings are then given by $P_T(t) = \cos^2(\Delta t)$ and $P_B(t) = \sin^2(\Delta t)$ respectively. Defining τ_C as the time required for the electron to complete one circulation about the rings, it takes the electron $N = \pi/(2\Delta\tau_C)$ circulations to transfer from one ring

to the other.

Consider the setup in Figure 2-4: an electron is injected into the top ring trap (initially prepared in $|T\rangle$), and an object composed of opaque and transparent regions (i.e. pseudo black and white pixels as discussed earlier) crosses the electron's path in the bottom ring. Again, opaque (transparent) regions have a probability of electron transmission near zero (one). It should now be mentioned that this opaque and transparent idealization is reasonable with regard to the electron imaging system of interest as in high-energy TEM, staining or immunolabelling thin specimens with heavy metal solutions or metal nanoparticles allows one to achieve significantly high-contrast transmission (see Figure 2-4 part b), where metals almost completely block electron transmission while the rest of the thin specimen becomes highly transparent to electrons at high kinetic energies [17].

With a transparent region of the object in the bottom ring (i.e. a white pixel in Fig. 2), the evolution of the circulating electron wavepacket is unaffected. After N circulations the electron transfers entirely from state $|T\rangle$ to state $|B\rangle$ i.e. the probability of measuring the electron in $|B\rangle$ after N circulations given the presence of a transparent region is $P(B|\text{transparent}) = P_B(N\tau_C) = 1$.

If an opaque region of the object (i.e. a black pixel in Fig. 2) blocks the electron's pathway, however, the coherent transfer of the electron between the rings is prevented. This is again just a manifestation of the quantum Zeno effect. After being injected into the top ring the electron begins to evolve from $|T\rangle$ to $|B\rangle$, but after a time τ_C the presence of the opaque region forces a measurement on the spatial state of the electron. If $\Delta\tau_C$ is small (i.e. N is large), the electron's wavefunction is projected back to the top ring with a high probability of $P_T(\tau_C) = \cos^2 \Delta\tau_C \approx 1-\pi^2/4N^2$. With each circulation around the ring, this measurement process is repeated, and after N circulations the electron remains in $|T\rangle$ with a probability of $P_T(\tau_C)^N = \cos^{2N} \Delta\tau_C \approx 1-\pi^2/4N$. Thus, after N circulations and given the presence of an opaque region, the probability of measuring the electron in $|T\rangle$ is $P(T|\text{opaque}) = P_T(\tau_C)^N \approx 1-\pi^2/4N$, and the probability of the electron being absorbed or what will from now on be referred to as scattered by the object is $P_{scat=1-P(T|\text{opaque})\approx\pi^2/4N}$.

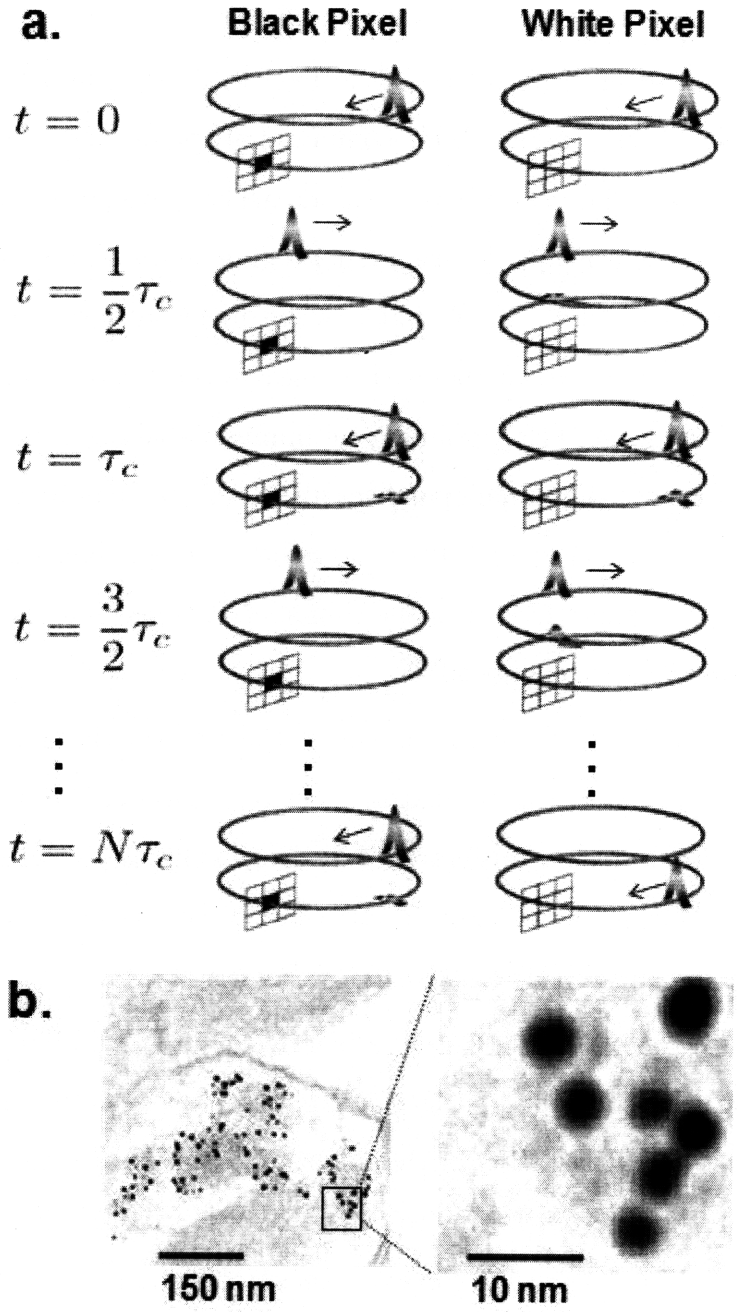

Figure 2-4: Interaction-free Imaging with Electrons. a. The grid in the lower ring is the object being imaged, which is composed of opaque and transparent regions (i.e. black and white pixels). b. Example of high-contrast TEM imaging at 100 keV. Gold nanoparticles labeled with antibody against vesicular monoamine transporter appear as black dots while the rest of the tissue in the background is significantly transparent to the incident electrons. The image contrast is reduced to make the background visible. Image courtesy of Kathryn Commons of Harvard.

By measuring which ring the electron is in after N circulations, the presence of an opaque or transparent region of an object in the bottom ring can then be determined with vanishing probability of scattering from the object. An image of an object composed of opaque and transparent regions can then be generated by rastering the object across the electron's path in the bottom ring where the electron beam width in the r-z plane dictates the pixel resolution.

The efficiency η of this interaction-free imaging can now be calculated. Assuming (as always in this work) the *a priori* probabilities of a region being opaque or transparent are equal i.e. $P(\text{opaque}) = P(\text{transparent}) = 1/2$, the efficiency takes the typical form, $\eta = \frac{1}{2}\left(P(T|\text{opaque}) + P(B|\text{transparent})\right)$. For the system in the preceding discussion, the efficiency is then (note the similarity between this efficiency and that for the high-efficiency IFM interferometer),

$$\begin{aligned} \eta &= \frac{1}{2}(1 + \cos^{2N}(\Delta\tau_C)) \\ &\approx 1 - \frac{\pi^2}{8N} \end{aligned} \tag{2.10}$$

The scattering probability also follows simply,

$$P_{scat} = 1 - \cos^{2N}(\Delta\tau_C) \approx \frac{\pi^2}{4N} \tag{2.11}$$

By making N large, this efficiency can be made arbitrarily close to one and the scattering probability can be made arbitrarily close to zero: opaque and transparent regions can be distinguished with arbitrarily high probability without scattering.

In concluding this chapter, the overall simplicity of the above scheme should be stressed once more. The basic concept is very simple. Two ring shaped electron guides are coupled such that for an electron in the rings each circulation results in a small portion of the electron's wavefunction tunneling from one projection state to the other as the two-state system coherently evolves from one ring to the other. However, with an inhibiting object, i.e. a black pixel, blocking a portion of one of the rings this coherent tunneling is prevented, and the electron will remain in the initial

projection state.

The above sketch of a design constitutes a high-efficiency IFM scheme that may be amenable for use with electrons. The main possible hinderances are technical issues associated with designing the electron ring guides and issues concerning quantum decoherence effects. These two main area are discussed in the following Chapters 3 and 4 respectively.

Chapter 3

Electron Trap Design

In the preceeding chapter a design was presented for an electron based IFM implementation that may present a route towards non-destructive electron microscopy. A key element to this general design was an electron trapping structure that could stably confine electrons and allow for them to coherently tunnel. In this chapter the basics of electron, and more generally charged particle, confinement are briefly reviewed in the context of the common radiofrequency quadrupole Paul trap, and then the requirements specified by the electron IFM design are met through a novel combined (hybrid Paul-Penning) trap structure.

3.1 Introduction to Charged Particle Traps

The non-trivial nature of the problem of trapping a charged particle is easy to understand. From Gauss's law in electrostatics the divergence of the electric field in a charge-free region vanishes, $\vec{\nabla} \cdot \vec{E} = 0$. Since $\vec{F} = Q\vec{E}$, where Q is the particle charge, the divergence of the force on a charged particle due to an external field must vanish as well, $\vec{\nabla} \cdot \vec{F} = 0$. Therefore, there can be no local minima in the force-field the particle sees. This is a simple result for harmonic functions from complex analysis, and in the context of electrostatics is known as Earnshaw's theorem [18]. The stable confinement of a charged particle is thus not an entirely simple problem, and radiofrequency fields or combinations of magnetic and electric fields must be used for

confinement.

Most common charged-particle traps can be divided into two main categories: Paul Traps and Penning Traps. Paul traps (also referred to in the following as quadrupole RF traps) exploit radio-frequency fields to create a stable potential minima to confine particles. Penning traps use a combination of electric and magnetic fields to confine charges. In the following design a hybrid Paul-Penning trap, known as a combined trap, will be used for electron confinement. While the underlying physics of the Penning trap can be analyzed in a relatively straighforward fashion, the electrodynamics and quantum mechanics of the Paul trap becomes complicated because of the time-varying nature of the potential. However, by way of a simple approximation, the physics of this oscillating potential can be summarized compactly in a static pseudopotential or effective potential [19, 20]. This approximation will be essential for the following discussion, and thus before going further this fundamental approach will be reviewed.

Imagine a mass M with charge Q moving in an inhomogeneous high-frequency electric field. Consider the motion of the particle (following [21]) in a field having static component $E_0(x)$ and high-frequency component $E_\Omega(x,t) = E_\Omega(x)\cos\Omega t$ such that, although $|E_\Omega| \sim |E_0|$, the amplitude of the particle oscillation uner the action of E_Ω is small. This is known as the *adiabatic condition* [20]. The motion of the particle will then consist of a small amplitude oscillation, or micromotion, at frequency Ω superimposed over some smooth average motion, or secular motion. The position coordinate of the particle can then be denoted,

$$x(t) = X(t) + \zeta(t) \tag{3.1}$$

Where $X(t)$ is the secular motion, and $\zeta(t)$ is the micromotion. Expanding the field in powers of ζ and keeping only linear terms, the following equation of motion is obtained,

$$\frac{d^2X}{dt^2} + \frac{d^2\zeta}{dt^2} = \frac{Q}{M}\left(E_0 + \zeta\frac{dE_0}{dx} + E_\Omega\cos\Omega t + \zeta\frac{dE_\Omega}{dX}\cos\Omega t\right) \tag{3.2}$$

The crucial step in the effective potential development is then to identify that the rapidly oscillating and smoothly varying terms must seperately satisfy the equation. This results in,

$$\frac{d^2X}{dt^2} = \frac{Q}{M}E_0 - \frac{Q^2}{M^2\Omega^2}\langle E_\Omega \frac{dE_\Omega}{dX}\cos^2\Omega t\rangle \tag{3.3}$$

Where the brackets denote a time average. It then simply follows that the secular motion is determined by an effective potential or pseudopotential,

$$U_{eff} = U_0 = \frac{Q}{4M\Omega^2}E_\Omega^2 \tag{3.4}$$

As it turns out not just the classical trajectory, but the quantum mechanics inside the trap can be accurately approximated by this pseudopotential for both normal Paul [22] and combined type traps [23]. However, in analyzing the quantum or classical mechanics of a charged particle in a trap in the context of the pseudopotential, care must be taken to ensure that the appropriate assumptions are met [24]. Now that the problem of charged particle trapping and the basic physics have been introduced, the relevant trap structures for the following design will be presented.

3.2 The Linear-Planar Paul Trap

The Paul trap is a charged particle trap which relies on radiofrequency electric fields to produce a stable pseudopotential minima for a confined particle. Since the pseudopotential is proportional to the square of the amplitude of the oscillating field, it is logical to oscillate a quadrupole field, as such a field will lead to a simple harmonic restoring force. The appearance of this harmonic restoring force can easily be understood by looking at the quadrupole potential, $\phi = \gamma(Ax^2 + By^2 + Cz^2)$, where $A+B+C = 0$ to satisfy Laplace's equation. The electric field will be proportional to the gradient of this potential, and the ensuing square magnitude of the field, which is proportional to the pseudopotential, will clearly create a harmonic type potential. The quadrupole field used by Paul traps can be very accurately created using hy-

perbolic electrode surfaces. However, more practical rod or box electrodes can also be used as such structures create a dominantly quadrupole moment near their center [19, 20].

The linear trap is a particular kind of Paul trap in which the RF fields are used to create a pseudopotential minima in a plane, for example the $x - y$ plane, and the particle is free or confined by a simple static field in the third orthogonal direction, the z-direction for example [Ghosh95,Major05]. An illustration of the electrode structure for a simple linear Paul trap is shown in Figure 3-1. Also in Figure 3-1, the effective potential created by the four-rod linear Paul trap is illustrated.

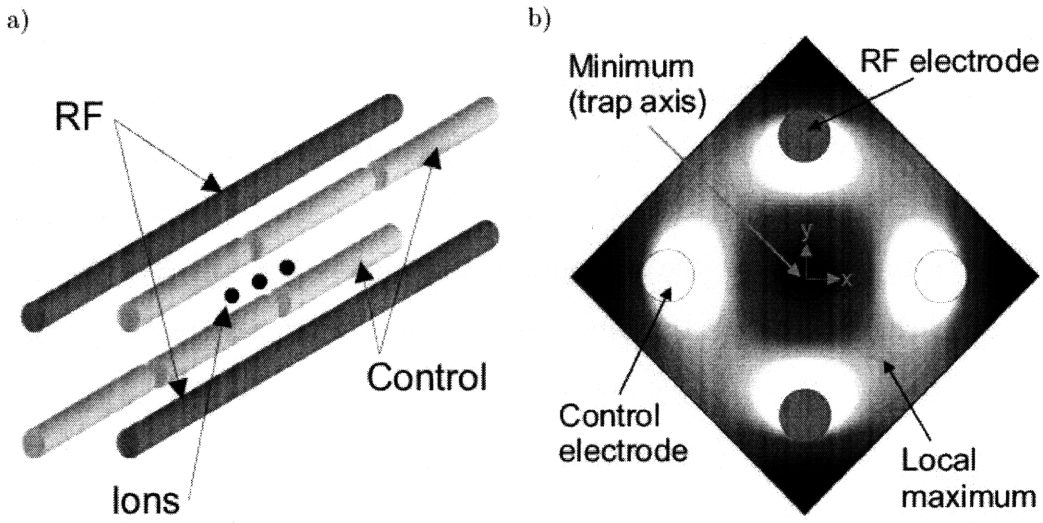

Figure 3-1: Paul Trap Basics. a. Illustration of the arrangement for a simple four-rod linear Paul trap [25]. b. The effective potential formed by such a four-rod structure [25]. The black indicates low potential and the lighter shades are increasing values of potential with white being a cutoff value.

Recently it was demonstrated that the perfect hyperbolic geometry and its variants such as the four rod geometry shown in Figure 3-1 could be deformed drastically and a strong quadrupole moment could still be maintained [25]. Exploiting this property, linear Paul traps in which all the electrodes lie in a single plane have been constructed [26, ?]. These linear-planar Paul traps will be used to create the particular trap structure for the electron based IFM design. The effective potential for a linear-planar Paul trap is presented in Figure 3-2.

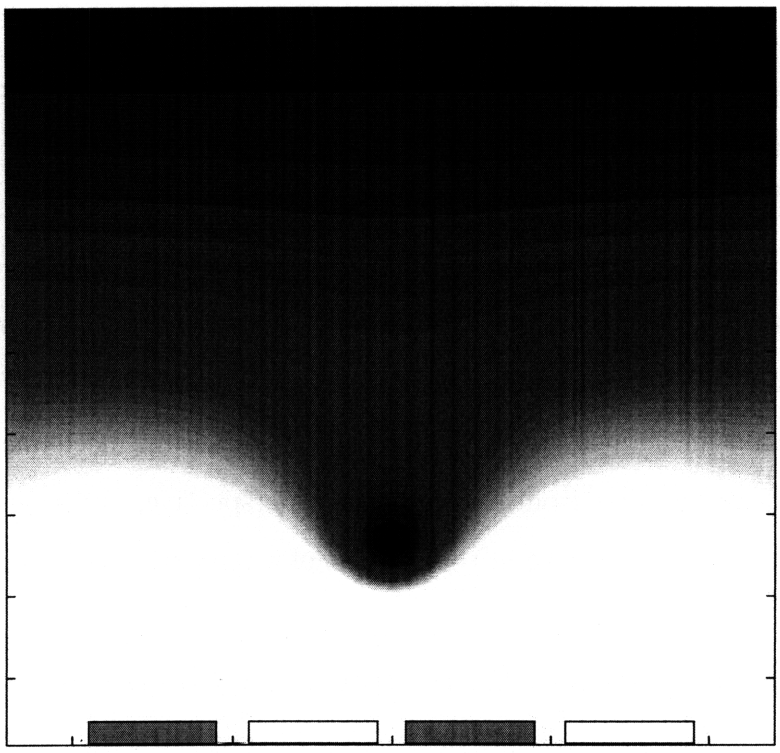

Figure 3-2: Linear Planar Paul Trap Effective Potential [25]. The gray electrodes are RF and the white are DC (ground). Again black indicates low potential and the lighter shades are increasing values of potential with white being a cutoff value.

3.3 The Combined Trap

The combined trap is hybrid Paul-Penning trap. It uses radiofrequency electric fields and a magnetic field to confine charged particles. The functionality of the combined trap is most easily understood from the perspective of a Penning trap. The Penning trap uses a static quadrupole field to confine charged particles in an axial direction. In the radial direction this quadrupole field is repulsive. However, if a magnetic field is applied and aligned with the axis of confinement, then the Lorentz force will act to return escaping particles, and charged particles will orbit in epitrochoids around the axis of confinement. An epitrochroid is the path traced by a point on a circle rolling around another circle. The motion that results from the small, rolling circle is called the cyclotron motion, and the motion from the larger, static circle is called the magnetron motion.

The combined trap is essentially a Penning trap with RF, instead of static, poten-

tials applied to the electrodes. With the RF potentials the force on the charge at the center of the trap is no longer repulsive in any direction. The combined trap applies the strong confinement of a Paul trap to a Penning trap. The trap structure design for electron IFM that follows is a combined trap, but its operation will most resemble that of a Paul trap. The quantum mechanics however will be more detailed than those of the Paul trap because of the additional magnetic field. In this way, while the operation is Paul-like, the quantum mechanics is more a combination of the Paul and Penning quantum mechanics. In the following, the quantum mechanics of the combined trap is discussed first from a Penning-like perspective, and then from a more useful coherent state perspective in the context of a semiclassical approximation.

3.3.1 Basic Combined Trap Quantum Mechanics

The quantum mechanics in the combined trap becomes more sophisticated than that in the Paul trap because of the addition of a magnetic field. The following discussion follows closely [20] but uses the effective potential following [23]. Take a particle of mass m and charge $-e$, an electron, confined in a combined trap with effective potential $U_{eff}(r,z)$ (working in cylindrical coordinates). The Hamiltonian for this system can be written,

$$H = \frac{1}{2m}(\vec{p} + e\vec{A}) + U_{eff}(r,z) \tag{3.5}$$

Where $\vec{p} = -i\hbar\vec{\nabla}$ is the momentum operator and $\vec{A}$ is the vector potential. If the magnetic field is aligned along the $\hat{z}$ direction, $\vec{B} = (0,0,B_0)$, then this vector potential can be written in the Coulomb gauge as $\vec{A} = \frac{B_0}{2}(0,r,0)$. Plugging in these expressions, the Hamiltonian becomes,

$$H = -\frac{\hbar^2}{2m}\vec{\nabla}^2 + \frac{1}{8}m\omega_c r^2 - \frac{i\hbar\omega_c}{2}\frac{\partial}{\partial\theta} + U_{eff}(r,z) \tag{3.6}$$

Where the cyclotron frequency has been defined as $\omega_c = eB_0/m$. Now this Hamiltonian is not amenable to a typical separation of variable scheme since the $\partial/\partial\theta$ term (proportional to the $\hat{z}$ componenet of angular momentum) couples the radial

coordinate with the angular one. A typical remedy to this coupling is to go into the eigenbasis of L_z and separate solutions to the time-independent Schrödinger equation like $\psi_l(r,\theta,z) = r^{-1/2}R_l(r,z)\exp(-il\theta)$. The downside to this method is the direct correspondence between the classical and the quantum seems lost as now the electrons are expressed as plane waves spread out on a ring, and although a superposition of such plane waves could give a simple wavepacket picture, that would require solving the Schrödinger equation for ψ_l for many different values of l. Additionally, although it is not transparent from the above formulation, the solutions expressed as plane waves in the $\vec{\theta}$-direction result in solutions to the radial part of the equation that in no obvious way converge in the appropriate summation to the semiclassical wavepacket picture.

3.3.2 Coherent States in the Combined Trap

The preceding discussion demonstrated the need for an alternative to the ordinary separation of variables approach to the combined trap quantum mechanics. Such an alternative is demonstrated in the following section in which a clear picture of the wavepacket mechanics of the problem is presented in a kind of semiclassical formulation. It is similar to the development of coherent states in a simple electron cyclotron orbit about a constant magnetic field as presented in [27].

Take the Hamiltonian developed in the preceeding section, equation 3.6. Instead of moving to the eigenbasis of L_z and seperating solutions, the solutions to the time-dependent Schrödinger equation can be written in the form,

$$\psi(r,\theta,z) = \exp(-i\omega_c t\frac{\partial}{\partial\theta})r^{-1/2}\phi(r,\theta,z)T(t) \tag{3.7}$$

Plugging this solution in to the time dependent equation and canceling the exponential factors, the resulting Hamiltonian is then similar to the form of equation 3.6, but with the sign in front of the $\partial/\partial\theta$ term flipped,

$$H = -\frac{\hbar^2}{2m}\vec{\nabla}^2 + \frac{1}{8}m\omega_c r^2 + \frac{i\hbar\omega_c}{2}\frac{\partial}{\partial\theta} + U_{eff}(r,z) \tag{3.8}$$

The impact of this sign flip is not immediately obvious; however, the function of the exponential factor can be understood physically. The exponential factor can be rewritten as $\exp(\omega_c t L_z/\hbar)$. This term is just the familiar rotation operator. It rotates a ket about an angle $\omega_c t$. Therefore, the rotation operator that was applied just serves to force the electron to circulate the ring at the classical cyclotron frequency. After seperating the temporal and spatial components of the remaining solution, the Schrödinger equation reads,

$$\begin{aligned} E\phi(r,\theta,z) &= -\frac{\hbar^2}{2m}\left(\frac{\partial^2}{\partial r^2}+\frac{\partial^2}{\partial z^2}\right)\phi(r,\theta,z)+\frac{L_z^2}{2mr^2}\phi(r,\theta,z)-\frac{\hbar^2/4}{2mr^2} \\ &\quad -\frac{1}{2}\omega_c L_z\phi(r,\theta,z)+\frac{1}{8}m\omega_c^2 r^2\phi(r,\theta,z)+U_{eff}\phi(r,\theta,z) \end{aligned} \tag{3.9}$$

Now a semiclassical approximation can be applied such that the quantum mechanics in $\vec{\theta}$-diretion is replaced by classical mechanics. This approximation is justifiable since the electron wavepacket in the IFM system will be moving at a high velocity in the $\vec{\theta}$-direction and therefore will have a very small wavelength and thus somewhat classical behavior in this direction. This semiclassical approximation functions to replace θ-dependent quantities with expected values and eliminate the θ-dependence of the Schrödinger equation. Mathematically this can expressed as,

$$\phi(r,\theta,z)=\sum_l a_l R_l(r,z)e^{-il\theta}\approx R(r,z)Y(\theta) \tag{3.10}$$

Then inserting this into the Schrödinger equation and multiplying by $Y^*(\theta)$ and integrating over θ, the resulting Schrödinger equation is,

$$\begin{aligned} ER(r,z) &= -\frac{\hbar^2}{2m}\left(\frac{\partial^2}{\partial r^2}+\frac{\partial^2}{\partial z^2}\right)R(r,z)+\frac{\langle L_z^2\rangle}{2mr^2}R(r,z)-\frac{\hbar^2/4}{2mr^2} \\ &\quad -\frac{1}{2}\omega_c\langle L_z\rangle\ R(r,z)+\frac{1}{8}m\omega_c^2 r^2 R(r,z)+U_{eff}R(r,z) \end{aligned} \tag{3.11}$$

Now the expected values of L_z and L_z^2 can be replaced with the corresponding

expected values of the mechanical angular momentum, L_{mck}. The canonical angular momentum is related to the mechanical angular momentum in this case by the simple relation $L_z = L_{mck} - \frac{eB_0}{2}r^2$. After this replacement the complete potential the semiclassical electron feels can be written as,

$$V(r,z) = \frac{\langle L_{mck}^2 \rangle}{2mr^2} + \frac{1}{2}m\omega_c^2 r^2 + U_{eff}(r,z) \tag{3.12}$$

Where the $\hbar^2/8mr^2$ term has been neglected since it is much smaller than the semiclassical centripetal potential contribution. This potential takes a very simple form of a centripetal component plus a confining magnetic component. It also gives the correct cyclotron orbit radius and wavepacket behavior that naturally corresponds with the expected classical motion. The above development will be important in the following discussion of the trap design for electron IFM.

A final important note concerning the potential given above is that in the radial direction the electron is confined in part by the magnetic portion, which looks like a harmonic oscillator of frequency ω_c, and in part by the radial confinement provided by the effective potential $U_{eff}(r,z)$. In the following trap design the cyclotron frequency is far greater than the effective frequency of the effective potential in the radial direction, so the dominant term in the radial potential is due to the magnetic confinement. This is important because if the potential can be approximated as the sum of a radially dependent term and a axially dependent term then the solutions can be seperated again. This time into a radial and axial part.

3.4 The Double-well Combined Trap

In the electron IFM design, a system more complicated than a normal electron trap is necessary. A structure that can stably confine high velocity electrons and allow for coherent tunneling of the electrons between two trapped states is required. In the following, the tunneling of an electron between a double-well potential is reviewed to get a feel for the length and energy scales requisite for coherent tunneling at a high rate. Then an actual trap structure that will allow such tunneling and confinement

is presented.

3.4.1 Double-well Tunneling

Briefly returning to the quantum mechanics of the combined trap, it was mentioned in the previous section that the strong magnetic confinement of the electron allows the separation of the Schrödinger equation into a radial and an axial part. This means that if the effective potential takes on some complicated double-well form in the $\hat{z}$-direction then the tunneling rates can be solved by simply looking at the analagous one-dimensional problem. Therefore, in the following discussion of tunneling only the one-dimensional case is considered.

Consider a double-well potential where ω is the characteristic frequency of the two wells when they are far apart, and the two potential minima are located at $\pm a$. Such a potential can be written as,

$$V(x) = \frac{m\omega^2}{8a^2}(x-a)^2(x+a)^2 \tag{3.13}$$

This is the canonical double-well potential, and there are a variety of different theoretical treatments. The two most popular of these theoretical treatments are the semiclassical WKB approximation and the path-integral based instanton approximation. The WKB method has inherent errors associated with the connection formulae [28], so the instanton approximation is more accurate [29].

The instanton approach involves Wick rotating the path integral description of the tunneling to imaginary time, and then looking at the resulting Euclidean path integral. If the dimensionless parameter η is defined as,

$$\eta = \sqrt{\frac{\hbar}{m\omega a^2}} \tag{3.14}$$

Then the instanton result can be summarized as [30],

$$\Delta E = \frac{4\hbar\omega}{\sqrt{\pi}\eta}\exp(-\frac{2}{3\eta^2}) \tag{3.15}$$

Where ΔE is the energy splitting between the ground state and first excited state in the double-well (that is the splitting between the first symmetric and anti-symmetric states). Now in the following chapter the imperfections of the electron IFM system will be discussed, and, summarizing the results for now, the coherent lifetime of the electron in the trap will be roughly 1 μs in the system. Using the above treatment of the tunneling problem, the desired length scale, a, and barrier height, $V_0 = m\omega^2 a^2/8$, can be estimated. The predicted length scale is roughly $a \sim 1\mu$m, and the predicted barrier height is around $V_0 \sim 10^{-7}$eV. Although these estimates are not entirely reliable (on the ns timescale and μm length scale the small η approximation inherent in the instanton approach breaks down), they provide a good starting point for the numerical approach in the following section.

3.4.2 The Double-well V-Trap

The requirements for the trapping structure in the electron IFM design are now clear. For tunneling, the trap must form two wells seperated by roughly several micrometers with an adjustable, and very low-noise, barrier in between. For more practical matters the trap should provide some open access so a sample can be inserted and rastered, and so electrons can be injected and detected. Additionally, the electrons must be able to move through the ring trap structures at a high velocity and maintain stability. These requirements can be met by combining two linear planar Paul traps into a v-type shape and adding a magnetic field.

The essential idea is to start with two adjacent linear planar Paul traps and then fold them towards each other, into a v, so that the trapping minima become close. It turns out this idea is feasible and creates a potential that in one direction looks strongly like the canonical double-well potential. Additionally, since the barrier arises in a somewhat natural sense (it is not due to an additional electrode), it is fairly resiliant to noise on the electrodes, and V_0 can be controlled at the level of 10^{-8}eV. A depiction of the geometry and of the effective potential are given in Figure 3-3.

Bending the v-shaped configuration into a circle, two ring traps coupled in a double-well can be made. For a ring radius of $\approx$1mm and typical TEM electron

energies of ≈100 KeV, the necessary centripetal force for circulation is considerale. However, a small magnetic field B_0 applied in the $\vec{z}$ direction (in this case $B_0 \approx 1$ T) can supply the required force and converts the Paul trap arrangement to a combined trap. Figure 3-3 depicts a cross-section of the effective potential of the v-shaped arrangement of ring shaped linear planar Paul traps.

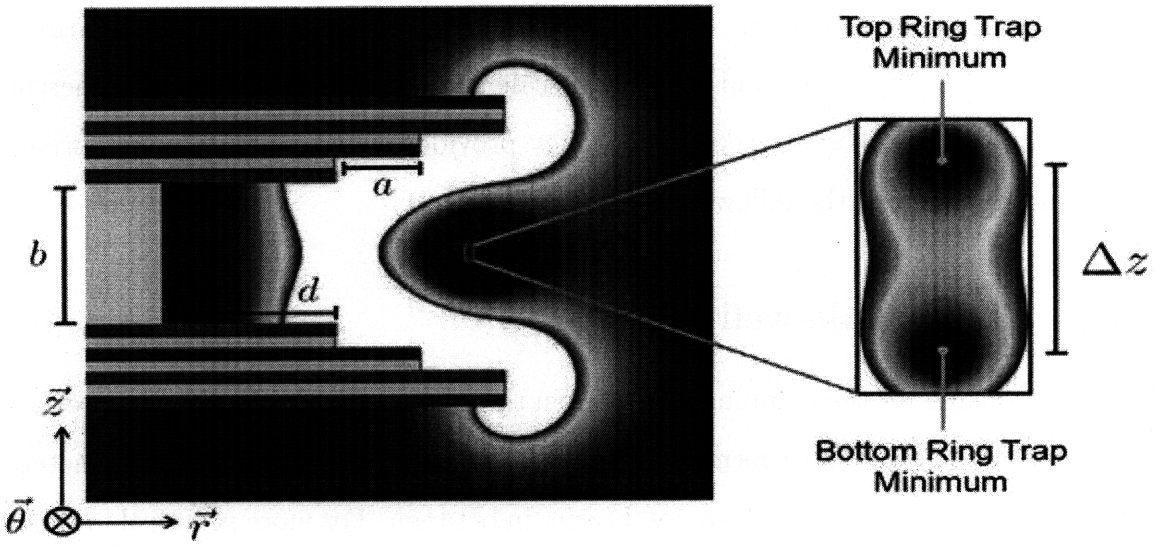

Figure 3-3: V-Trap Geometry and Effective Potential. The image depicts the multi-layered structure equivalent to the v-shaped trap arrangement but more suitable for microfabrication. The effective potential $U_{eff}(r, z)$ is superimposed on the structure; blue and red colors are low and high potentials, respectively, and white regions have potentials > 20 meV. Blue and red rectangles are grounded and RF electrodes (gold), respectively, and green is insulating silicon dioxide. The darker regions are lower potential and white is higher (with a cutoff). The inset shows an expanded view of the double-well.

For the trap depicted in Figure 3-3 the dimensions are $b = 48.5$ μm, $a = 24$ μm, and $d = 50$ μm. The electrode width and spacing are 4 μm. The RF voltage is driven at a frequency of 10 GHz with a magnitude of 2 V. Near the trap minima the potential is harmonic with characteristic frequencies of $f_r, f_z = 33$ MHz, yielding a tunneling rate of $\Delta' = 2\pi \times 14$ MHz and an electron spot size (i.e. resolution) of 19 nm and 1.4 μm in the $\vec{r}$ and $\vec{z}$ directions (accounting for $B_0 = 1$ T for $R = 1$ mm).

The dimensions of the trap, in particular the height b and the electrode width a (Figure 3-3), can be varied to adjust the positions of the trap minima. The magnitude of the applied oscillating voltage can be used to tune the tightness of the trap i.e. the trap's characteristic frequencies f_r and f_z. Also since the tunneling depends only on the proximity of the two traps and their strengths, the influence of the electrode voltage noise on the tunneling time is small. For the example trap, a fluctuation of 100 μV on one electrode results in only about 1% change in the tunneling time.

The simulations were carried out in a standard finite-element solver COMSOL which was interfaced and looped through an extensive MATLAB routine. Many different geometric variations were simulated as well as many different cases involving noisy electrodes. The v-trap structure is fairly sensitive to geometric variations (to around the 100 nm scale) and fairly insensitive to noisy electrodes.

The double-well combined trap composed of a revolved version of the proposed v-type trap satisfies all the criteria for electron trapping required by the electron IFM design, and may be used to make this design possible. In the next chapter possible deficiencies of this trap arrangement are discussed. Namely the effect of environmental interactions on the coherent quantum process that occurs in the trap is analyzed.

Chapter 4

Design Considerations

In the previous chapter an electron trapping structure that may be capable of confining and coherently splitting electrons for the presented electron IFM design was presented; however, like any design, the trap has inherent limitations and imperfections which restrict the achievable efficiency of the system. The following chapter gives an analysis of the dominant limitations and imperfections: decoherence and heating. Additionally, the performance of the electron IFM system with the presented trap structure in the presence of these imperfections is predicted.

4.1 Decoherence

Decoherence is the unavoidable emergence of classical features in quantum systems due to interaction with the environment. The theory of decoherence is deep and rich and, over the past two decades, has given new insight into some fundamental axioms of quantum mechanics [31]. The theory describes the manner in which quantum systems become effectively classical, so techniques from decoherence theory will be used in the following discussion to determine how long an electron in the designed trap structure can be maintained in a coherent spatial superposition before classical behavior dominates. The main sources of decoherence in the design are determined, and the resulting timescale for the decoherence of spatially spread electrons in the trap is found. Additionally, a brief discussion of the impact of decoherence on the

overall efficiency of the system is included.

4.1.1 Image-Charge Decoherence

In the microtrap system the a major source of decoherence will be through image charge production and dissipation. As the electron travels around the ring it induces an image charge in the trap electrodes which moves along with it producing a current in the conductor. This current encounters Ohmic resistance due primarily to electron scattering in the metal by thermal phonons. The resulting Joule heating and dissipation disturbs the quantum state of the electron/phonon gas in the metal. The location of this disturbance depends on whether the electron is in the top or bottom ring, and thereby the disturbance provides some amount of which path information which results in the decoherence of the spatial superposition [32, 33]. The essential problem (not any particular portion of the design) is depicted in Figure 4-1.

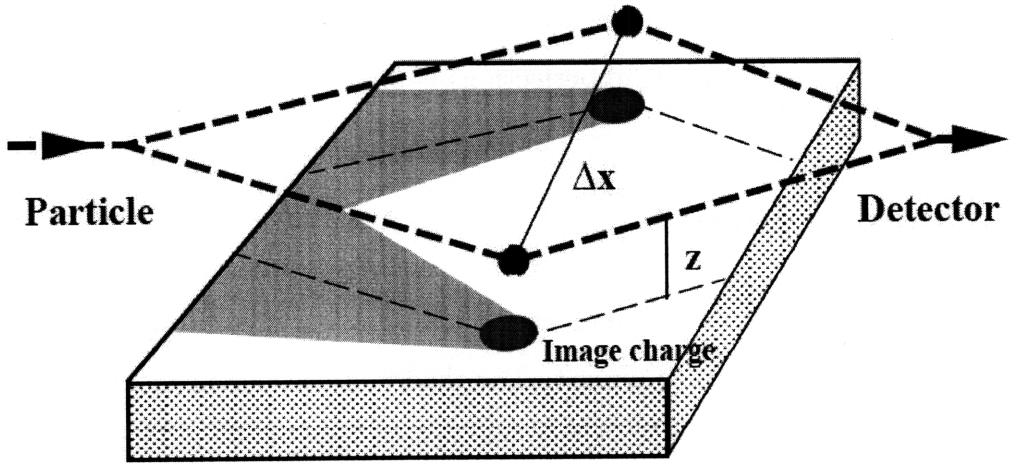

Figure 4-1: A charge passes over a conducting plate at height z and is spatially superimposed over a distance Δx [33]. An image charge gas is produced at the surface of the conductor, and the trace left by each respective path results in decoherence of the spatial superposition.

This image charge decoherence can be phrased in a transparent mathematical framework. Using the parameters defined in Figure 4-1 and following [33], the joint

wavefunction that describes the state of the electron and the electron-phonon gas in the metal can be written as $|\Psi\rangle$. The contribution to this joint wavefunction from the electron taking a single trajectory, T, is

$$|\Psi_T\rangle = |x_f\rangle\,|\psi_E[T]\rangle \tag{4.1}$$

where $|x_f\rangle$ describes the final position of the electron. Then, using the path integral picture, the total joint wavefunction is described by a sum of all such contributions from each path, so the probability of measuring the electron's position at final position x_f is just,

$$P(x_f) = \sum_{x_i,x_i'} \phi(x_i)\phi^*(x_i') \times \sum_T \sum_{T'} \exp(\frac{i}{\hbar}(S[T] - S[T'])) \,\langle\psi_E[T]|\,|\psi_E[T']\rangle \tag{4.2}$$

where x_i and x_i' are initial positions of the electron, ϕ describes the electron's initial wavefunction, and T and T' are the trajectories being summed over. It's clear that when $\langle\psi_E[T]|\,|\psi_E[T']\rangle$, the overlap of the wavefunctions of different trajectories, is unity the expected interference from quantum mechanics results when the superimposed electron wavepackets are recombined. This corresponds to the case when the conducting plate does not distinguish at all between the different trajectories, hence their wavefunctions overlap entirely. However, when the plate does disntinguish between the paths the overlap term is reduced and the interference is slowly destroyed. This, described in the relevant context of image charge production, is the general mechanism of decoherence. Environmental interaction selects certain states and destroys interference.

Now that a general physical picture for image charge decoherence has been presented the actual impact of image charge decoherence in the IFM design will be discussed. The action of this image charge decoherence effect on the spatial superposition of an electron has been theoretically analyzed [33, 34] and experimentally investigated [32]. From a general perspective, a timescale for decoherence resulting from a dissipative process can be obtained from the classical relaxation time, τ_r, of

the dissipation with the relation [33, 14],

$$\tau_d = \tau_r \left(\frac{\lambda_{dB}}{\Delta x} \right)^2 \tag{4.3}$$

Where $\lambda_{dB} = h/\sqrt{2mkT}$ is the thermal deBroglie wavelength and Δx is again the distance over which the quantum coherence is maintained (in the electron IFM case, the separation between trap centers). Using the classical image charge dissipation rate [35] the decoherence lifetime from image charge dissipation can be estimated as [33],

$$\tau_{d,imag} = \frac{4h^2 z^3}{\pi e^2 kT \rho (\Delta x)^2} \tag{4.4}$$

Where z is, again, the distance from the electron superposition to the trap electrode under consideration (each electrode will have an image charge and result in decoherence), and ρ is the resistivity of the electrodes. In the proposed system this formulation of the decoherence time gives $\tau_d \sim 50\mu$s for the v-trap proposed in Chapter 3.

The above analysis was a general one, and it relied on the dominant decoherence mechanism being the actual dissipation due to the dragging of an image charge. Recently a many-body quantum calculation [34] estimated the dominant decoherencence mechanism to be due to the production of the image charge itself. This analysis gave a decoherence timescale of,

$$\tau_{d,imag} = \frac{64\epsilon_0 \epsilon_i \hbar z^2 k_F}{e^2} \left(\frac{\lambda_{dB}}{\Delta x} \right)^2 \tag{4.5}$$

Where k_F is the Fermi wavevector of the conductor, and ϵ_i is the ion dielectric constant of the conductor. Using this formula in conjunction with a conservative scaling of the experimental results for image charge related decoherence over semiconductors [32] predicts $\tau_{d,imag} \approx 11$ μs for the v-trap system desribed in Chapter 3 with a cryogenic electrode temperature of $T \approx 6$ K (cryogenic surface electrode traps operating at 6 K have recently been demonstrated [36]).

It should be noted that the decoherence lifetime is relatively high (μs instead of ns) because the length of the spatial superposition is much smaller than the length from the trapping centers to the electrodes. This is another feature of the trapping structure presented in the Chapter 3 that makes it such a favorable one.

4.2 Heating

Another detrimental effect is electron heating in the trap. Heating occurs when the trapped electron experiences fluctuating forces due to the noisy fields generated by the electrodes. When the spectrum of the noisy fields overlaps with the secular motion frequency of the trap or its micromotion sidebands, significant heating of the trapped electron may occur resulting in the electron decohering or actually leaping from the ground-state.

There are two main sources of noisy electric fields: Johnson noise due to the trap electrodes and external circuitry, and the fluctuating patch potentials due to random defects on the electrode surfaces [37]. The effect of these noise sources can be summarized in a scattering rate Γ_{0-1}, from the ground to the first excited state as [38],

$$\Gamma_{0-1} = \frac{e^2}{4m\hbar\omega_{sec}} S_E(\omega_{sec}) \tag{4.6}$$

where ω_{sec} is the secular frequency of the trap and $S_E(\omega_{sec})$ is the spectral density of the electric field fluctuations. A complete analysis of electron heating in the designed trap structure would be extremely involved and of limited use since the trap heating phenomena is poorly understood, and the spectral function $S_E(\omega_{sec})$ is difficult to define; however, scaling previous experimental findings for ion traps [37] by the dimensions and materials of the electron IFM design, the electron heating (the scattering rate, Γ_{0-1}) can be predicted to occur on a hundreds of micro to milli second timescale, sufficiently long for the proposed purposes since the tunneling occurs in nanoseconds. Although the heating is too weak to actually scatter the electrons significantly in the timescales over which the tunneling occurs the coupling of the elec-

tron to the fluctuating heating fields can result in rapid electron decoherence. Scaling heating rates measured in similar low-temperature surface-electrode traps [36] to the trap parameters specified in Chapter 3 and using the relationship between decoherence and heating rate [37] yields a decoherence time of $\tau_{d,heat} \approx 2$ μs. It should be noted however that this conservative estimate is dependent on fabrication process [36], so future improvement may be possible.

Although scaling of previous experimental results may give reasonable estimates, the effect of the patch potential noise is difficult to treat because of the variabilities in the actual effect and because of the difficulties in modeling the patch potentials. An approximate upper limit on patch potentials is ~100 mV [39], although it can be made lower. Assuming $z \sim 50\mu$m, the force acting on the electron from a patch is $F \sim 3.2 \times 10^{-16}$N. With an interaction time of around .1 ps (~patch size/electron velocity), this results in a momentum kick of $p_{kick} \sim 3.2 \times 10^{-29}$. Since this momentum kick is much smaller than the momentum required to scatter to higher states, $\Delta p = \sqrt{m\hbar\omega_{sec}/2} \sim 10^{-27}$Ns, the patch noise should not cause significant heating or scattering of trapped electrons over the small timescale dictated by the image-charge induced decoherence. Thus, electron trap heating does not pose any additional constraints on the system past those presented by decoherence; however, heating is important as a potential limitation as scaling the trap to much smaller dimensions could present serious heating effects.

4.2.1 Efficiency Limitations

In the preceding discussion decoherence timescales associated with two different environmental interactions were computed; however, the effect of these environmental interactions on the interaction-free measurement process was not calculated. This is done in the following.

When the coupling to the environment is sufficiently weak and the correlation time of the interactions is small, a set of Bloch-type equations can be written for the time evolution of the system's reduced density matrix [40, 41]. This follows by going into the density matrix description of the quantum dynamics of the system

of interest and simply appending damping terms to each off-diagonal element. The damping timescale is the decoherence time. Solving these equations for the electron based IFM design discussed at the end of Chapter 2 i.e. an electron initially prepared in the top ring of a coupled ring structure, the probabilities of an electron to be in the top versus the bottom ring can be found to be $P_T(t) = \frac{1}{2}(1+e^{-t/2\tau_D}\cos 2\Delta' t)$ and $P_B(t) = \frac{1}{2}(1-e^{-t/2\tau_D}\cos 2\Delta' t)$ respectively where τ_D is the decoherence time, and Δ' is the modified tunneling rate, $\Delta' = \sqrt{\Delta^2 - 1/16\tau_D^2}$.

Using these new expressions for $P_B(t)$ and $P_T(t)$, the efficiency in the presence of a decohering environment is found to be,

$$\eta(N,\alpha) = \frac{1}{2^{N+1}}(1+e^{-\alpha/2}\cos(\pi/N))^N + \frac{1}{4}(1+e^{-N\alpha/2}) \tag{4.7}$$

The dimensionless parameter $\alpha^{-1} \equiv \tau_D/\tau_C$ describes the decoherence strength. The probability of electron scattering by an opaque region (or the electron exposure reduction since exposure is proportional to scattering) after N circulations (given the presence of an opaque region) can likewise be found to be,

$$P(scat) = 1 - \frac{1}{2^N}(1+e^{-\alpha/2}\cos(\pi/N))^N \tag{4.8}$$

The image charge and heating induced decoherence rates can be combined in a single rate, $\tau_D^{-1} = \tau_{d,imag}^{-1} + \tau_{d,heat}^{-1}$, describing the decoherence due to environmental interactions. Using the worst-case decoherence estimates above, a conservative estimate for the decoherence time is $\tau_D \approx 1.7$ μs. Then with 100 KeV electrons, and a ring radius of either 1 cm or 1 mm gives α^{-1} values of 4.4×10^3 and 4.4×10^4, respectively. Refering to Figure 4-2, one finds corresponding scattering probabilities $P(scat)$ (and accuracies η) of 0.03 (0.98) for a ring trap radius of $R = 1$ cm and 0.01 (0.99) for a ring trap radius of $R = 1$ mm. Since sample exposure is proportional to electron scattering probability, this corresponds to two orders of magnitude reduction in sample exposure. Such a dramatic reduction in electron exposure could allow non-destructive imaging of molecular processes such as protein activity [42].

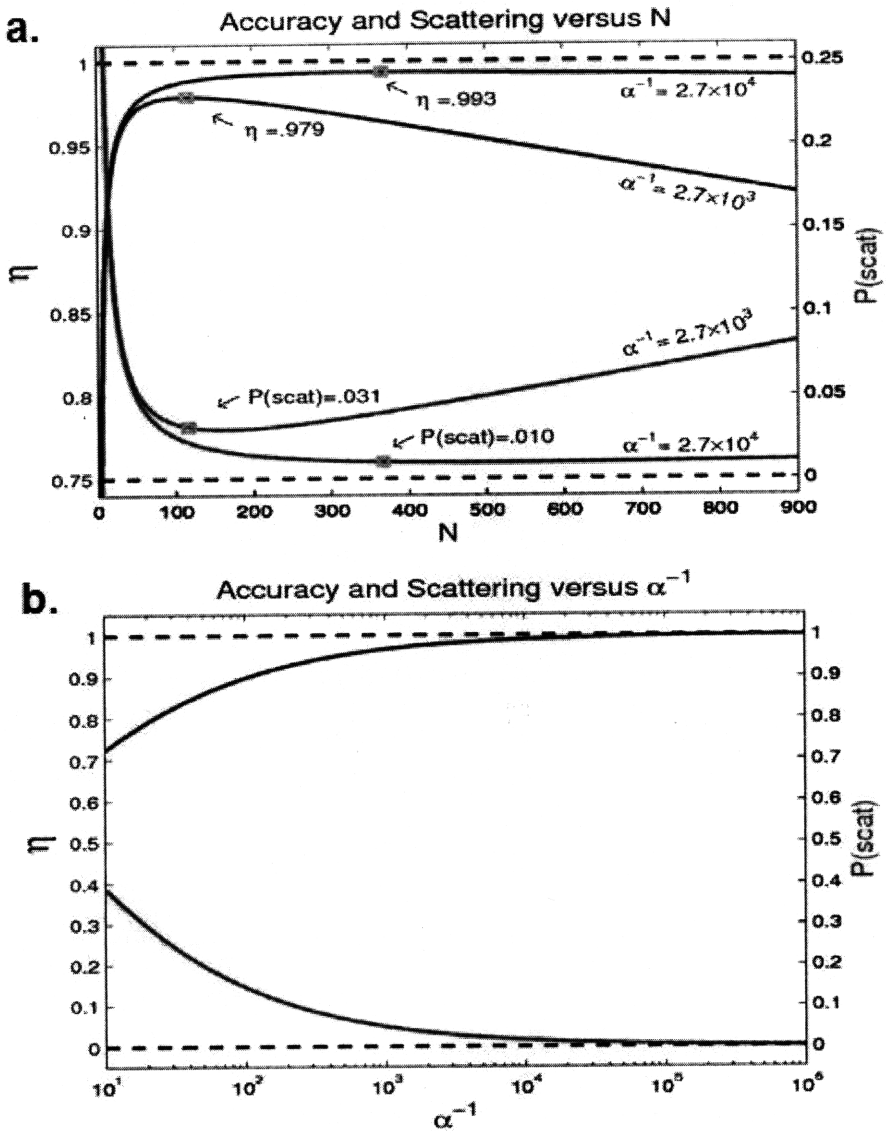

Figure 4-2: Efficiency of Interaction-free Measurement with Decoherence. a. The blue and red curves are plots of the imaging efficiency η and the probability of scattering $P(scat)$ versus N, respectively. The orange squares show points of maximum efficiency and corresponding values of scattering probability. The α^{-1} values 4.4×10^3 and 4.4×10^4 correspond to 100 KeV electrons circulating a ring of radius $R = 1$ cm and 1 mm respectively with a decoherence time of $\tau_D = 1$ μs. b. The blue and red curves are respectively the maximum values of η and the minimum values of $P(scat)$ as functions of α^{-1}.

Chapter 5

Conclusions

There are many engineering challenges that need to be overcome to make an electron IFM microscopy device practical. The major ones are electron injection and detection. For efficient injection of energetic electrons, one method could be direct injection of electrons from a single-electron field emission tip such as a carbon nanotube [43], and/or the use of a storage-ring in which electrons can be cooled by feedback techniques [44, 45] and then transferred to the imaging ring. Detection can most likely be done in a number of ways quite efficiently. One method could be to decrease the voltage on the top or bottom electrodes to eject the electrons outward or downward into scintillation material blocks or PIN-diode detectors. Additionally, to maintain electron beam coherence ultra high vacuum (UHV) conditions are necessary. Using chambers made of ultra thin membranes; biological specimen can be maintained fully hydrated under UHV conditions for electron microscopy [46, 47]. Beyond these engineering challenges, there is also an intrinsic limitation to the interaction-free detection of semi-transparencies (materials where the transmission amplitude for electrons is neither zero, opaque, nor one, transparent) [48].

Although there are challenges, overcoming these challenges does not seem entirely out of reach. Additionally, with the conceivably high efficiency of the electron IFM, the acquisition time per pixel of the imaging system could be made very small potentially allowing detection times on microsecond timescales, which may allow non-destructive imaging of dynamic molecular processes. In summary, the possibility of

non-destructive measurements with electrons even in the presence of worst-case electron decoherence rate estimates using an interaction-free measurement scheme based on charged particle trapping techniques has been shown. Interaction-free measurements with electrons can prevent sample exposure to highly energetic and destructive electrons in electron microscopy, which might allow noninvasive imaging of dynamic processes at molecular resolution, opening new frontiers in imaging.

Bibliography

[1] Ray F. Egerton. *Physical Principles of Electron Microscopy*, chapter 1. Springer, 2005.

[2] R. M. Glaeser and K. A. Taylor. Radiation damage relative to transmission electron microscopy of biological specimens at low temperature: A review. *J. Microsc.*, 112:127–138, 1978.

[3] D. T. Grubb and A. Keller. Beam-induced radiation damage in polymers and its effect on image formed in the electron microscope. *Proceedings of the 5th European Regional Conferences on Electron Microscopy, Manchester.*, pages 554–560.

[4] Robert A. Grassucci, Derek Taylor, and Joachim Frank. Visualization of macromolecular complexes using cryo-electron microscopy with fei tecnai transmission electron microscopes. *Nature*, 3(2):330–339, 2008.

[5] D. Gabor. Theory of electron interference experiments. *Rev. Mod. Phys.*, 28(3):260–276, 1956.

[6] M. Renninger. *Z. Phys.*, 158:417, 1960.

[7] A. Elitzur and L. Vaidman. *Found. Phys*, 23:987, 1993.

[8] Alan J. DeWeerd. *Am. J. Phys.*, 70(3):272–275, 2002.

[9] Eugene Hecht. *Optics.* Addison-Wesley, 2002.

[10] T. Tsegaye et al. *Phys. Rev. A*, 57(5):3987–3990, 1998.

[11] P. G. Kwiat et al. *Phys. Rev. Lett.*, 74:4763, 1995.

[12] Andrew G. White, Jay R. Mitchell, Olaf Nairz, and Paul G. Kwiat. *Phys. Rev. A*, 58(1):605–613, 1997.

[13] Meinrad Hafner and Johann Summhammer. Experiment on interaction-free measurement in neutron interferometry. arXiv:quant-ph/9708048v2.

[14] E. Joos, H.D Zeh, C. Kiefer, D. Giulini, J. Kupsch, and I.-O. Stamatescu. *Decoherence and the Appearance of a Classical World in Quantum Theory.* Springer, 2003.

[15] P. G. Kwiat et al. *Phys. Rev. Lett.*, 83(23):4725–4728, 1999.

[16] Harry Paul and Mladen Pavicic. *International Journal of Theoretical Physics*, 35(10), 1996.

[17] M. A. Hayat. *Principles and Techniques of Electron Microscopy: Biological Applications*. Cambridge University Press, 2000.

[18] David J. Griffiths. *Introduction to Electrodynamics*. Prentice Hall, 1999.

[19] Pradip K. Ghosh. *Introduction to Quantum Mechanics*. Oxford University Press, 1995.

[20] F. G. Major. *Charged Particle Traps*. Springer, 2005.

[21] L. D. Landau and E. M. Lifschitz. *Mechanics*. Butterworth-Heinemann, 1976.

[22] Richard J. Cook, Donn G. Shankland, and Ann L. Wells. *Phys. Rev. A*, 31(2):31–34, 1985.

[23] Li Guo-Zhong. *Z. Phys. D*, 10:451–456, 1989.

[24] M. Combescure. *Annales de L'I.H.P., Section A*, 44:293–314, 1986.

[25] Chiaverini et al. *Quantum Information and Computation*, 5(6):419–439, 2005.

[26] C. E. Pearson et al. *Phys. Rev. A*, 73:032307, 2006.

[27] S. Varro. *J. Phys. A: Math. Gen.*, 17:1631–1638, 1984.

[28] David J. Griffiths. *Introduction to Quantum Mechanics*. Prentice Hall, 2005.

[29] Chang Soo Park et al. Effect of anharmonicity on the wkb energy splitting in a double well potential. arXiv:quant-ph/9609008v1.

[30] Hagen Kleinert. *Path Integrals in Quantum Mechanics, Statistics, and Polymer Physics*. World Scientific, 1990.

[31] W. Zurek. *Rev. Mod. Phys.*, 75:715–775, 2003.

[32] Peter Sonnentag and Franz Hasselbach. *Phys. Rev. Lett.*, 98:200402, 2007.

[33] J. R. Anglin and W. H. Zurek. A precision test of decoherence. arXiv:quant-ph/9611049v2.

[34] Pawel Machnikowski. *Phys. Rev. B*, 73:155109, 2006.

[35] Timothy H. Boyer. *Phys. Rev. A*, 9(1):68–82, 1974.

[36] J. Labaziewicz et al. *Phys. Rev. Lett.*, 100:013011, 2008.

[37] Q. A. Turchette et al. *Phys. Rev. A*, 61:063418, 2000.

[38] C. Henkel, S. Potting, and M. Wilkens. *Appl. Phys. B*, 69:379–387, 1999.

[39] C. C. Speake and C. Trenkel. *Phys. Rev. Lett.*, 90(16):160403, 2003.

[40] A. J. Leggett et al. *Rev. Mod. Phys.*, 59:1–85, 1987.

[41] R. A. Harris and R. Silbey. *J. Chem. Phys.*, 78:7330, 1983.

[42] A. M. Glauert. *The Journal of Cell Biology*, 63:717–748, 1974.

[43] P. Hommelhoff et al. *Phys. Rev. Lett.*, 96:077401, 2006.

[44] B. D'Urso, B. Odom, and G. Gabrielse. *Phys. Rev. Lett.*, 90:043001, 2003.

[45] H. Dehmelt, W. Nagourney, and J. Sandberg. *Proc. Natl. Acad. Sci. USA.*, 83:5761–5763, 1986.

[46] S. Thiberge et al. *PNAS*, 101:3346–3351, 2004.

[47] http://www.quantomix.com/.

[48] G. Mitchison and S. Massar. *Phys. Rev. A*, 63:032105, 2001.